

Modelling the evolution of PAH abundance in galaxies

Shiau-Jie Rau^{1,2*}, Hiroyuki Hirashita¹, and Maria Murga³

¹*Institute of Astronomy and Astrophysics, Academia Sinica, Astronomy-Mathematics Building, AS/NTU, No. 1, Sec. 4, Roosevelt Road, Taipei 10617, Taiwan*

²*Department of Physics, National Tsing Hua University, Hsinchu 30043, Taiwan*

³*Institute of Astronomy, Russian Academy of Sciences, Pyatnitskaya str. 48, Moscow 119017, Russia*

Accepted XXX. Received YYY; in original form ZZZ

ABSTRACT

We investigate the evolution of polycyclic aromatic hydrocarbon (PAH) abundance in a galaxy, which is a crucial step to understand the evolution of bright emission features in the mid-infrared range. We calculate the evolution of dust grain size distribution in a manner consistent with the physical conditions of the interstellar medium by post-processing our previous hydrodynamical simulation of an isolated disc galaxy. We also differentiate between aromatic and non-aromatic grains for carbonaceous dust species and explicitly considered the aromatization process. As a consequence, our model explains the metallicity dependence of PAH abundances in nearby galaxies well. The PAH abundance increase is driven particularly by the interplay between shattering and accretion (dust growth). The fast aromatization guarantees that the small carbonaceous grains trace PAHs very well. Since shattering and accretion are sensitive to the dust abundance, we predict that the PAH-to-dust abundance ratio increases as the metallicity increases. This is consistent with the observation data of nearby galaxies.

Key words: dust, extinction — galaxies: evolution — galaxies: ISM — methods: numerical — ISM: molecules

1 INTRODUCTION

Mid-infrared (MIR) spectral energy distributions of galaxies usually have prominent emission features. Some of them are considered to be caused by carbonaceous species, which are likely to be polycyclic aromatic hydrocarbons (PAHs) (Leger & Puget 1984; Allamandola et al. 1985; Li & Draine 2012). There are some alternative candidates for the carriers of these emission features such as hydrogenated amorphous carbons (HAC; Duley 1993), quenched carbonaceous composite (Sakata et al. 1983), and mixed aromatic/aliphatic organic nanoparticles (Kwok & Zhang 2011). In this paper, we use PAHs to represent the materials responsible for the above MIR emission features.¹ PAHs play a key role in the energy balance of the interstellar medium (ISM) via absorbing ultraviolet (UV) photons and emitting in the MIR, and the ionization balance via interaction with electrons and ions (e.g. Tielens et al. 2008). The luminosities of these emission bands are also used as an indicator of star formation in galaxies (e.g. Förster Schreiber et al. 2004). Therefore, it is important to clarify the origin and evolution of PAHs in galaxies.

The luminosities of the MIR emission features show strong metallicity dependence (e.g. Engelbracht et al. 2005; Ciesla et al. 2014). The features are deficient in low-metallicity galaxies with

active star formation such as blue compact dwarf galaxies (e.g. Hunt et al. 2010). Hard UV spectra (Plante & Sauvage 2002) and/or enhanced supernova (SN) activities (O’Halloran et al. 2006) could play an important role in PAH destruction in low-metallicity environments. Madden et al. (2006) also suggested the importance of strong UV radiation field for PAH destruction (see also Madden 2000; Wu et al. 2006). However, the indication that the size distribution of PAHs are shifted to small sizes in the Small Magellanic Cloud may be in tension with the destruction scenario, which should produce the opposite trend in PAH sizes (Sandstrom et al. 2012). It is also possible that PAH evolution is strongly linked to the dust evolution. Young galaxies may not have sufficient time for asymptotic giant branch (AGB) stars to produce carbonaceous dust and PAHs and to supply them into the ISM (Galliano et al. 2008). Bekki (2013) also explained the metallicity dependence of PAH-to-dust ratio by AGB stars. However, Cherchneff et al. (1992) calculated PAH formation yields in carbon-rich stellar outflows and concluded that stellar outflows are not the main PAH formation sites. We should also note that the metallicity does not necessarily reflect the age (e.g. Kunth et al. 2000). Thus, the lack of PAHs in low-metallicity galaxies may not be simply due to the age effect. Since the metallicity dependence of the MIR features is also seen at high redshift ($z \sim 2$; Shivaee et al. 2017), it is important to clarify the physical reason for the strong link between PAHs and metallicity in the context of galaxy evolution.

Seok et al. (2014, hereafter S14) proposed a new idea to explain the metallicity dependence of PAH abundance. They modelled the evolution of the PAH abundance in galaxies by assuming

* E-mail: cherrymow@gapp.nthu.edu.tw

¹ Detailed identification of these spectral features is not important for this paper. As long as the emission features are attributed to small carbonaceous grains with aromatic structures, the scenario of this paper holds.

that small grain production by shattering is the source of PAHs. They also considered the destruction of PAHs by coagulation and SN shocks. However, S14 did not directly solve grain size distribution in their model but applied the Mathis et al. (1977, so-called MRN) grain size distribution to estimate the formation and destruction time-scales of PAHs. Using these time-scales, they post-processed the evolution of the total dust amount calculated by Asano et al. (2013a) and derived the evolution of the PAH abundance. In this sense, their PAH abundance evolution was not self-consistently calculated with the evolution of grain size distribution. Moreover, as shown by Hirashita (2012), shattering is not the only source of small grains: accretion drastically increases the small grain abundance, while S14 implicitly assumed that accretion keeps the shape of the grain size distribution. Thus, we aim at a self-consistent treatment of grain size distribution and PAH formation, although S14's basic idea that small-grain production leads to PAH formation still holds in this paper.

Another point worth improving is an explicit treatment of aromatization, which is a process of dehydrogenation under the influence of UV radiation. HAC grains have predominantly a disordered structure with aliphatic bonds between atoms. These bonds, especially C–H bonds, can be dissociated under UV radiation, and the number of hydrogen atoms in the HAC grains gradually decreases. This leads to the formation of aromatic bonds and aromatic ring structures. In this way, the structure becomes more ordered. Thus, PAHs can result from photo-processing of HAC grains, as also shown by experiments (Duley et al. 2015). The optical properties of the dehydrogenated HAC grains and PAHs are similar in the sense that they have the same emission bands in the MIR range. Since we are mainly interested in the abundance of aromatic emitters in this paper, it is not important which species, PAHs or HAC, is responsible for them. The essential points are (i) that there are aliphatic-dominated and aromatic-dominated species, and (ii) that aromatization converts the former to the latter ones. As mentioned above, we call small grains responsible for the MIR emission features as PAHs, keeping in mind that they can be HAC grains as well.

The purpose of this paper is to model the evolution of PAH abundance in a consistent manner with the evolution of grain size distribution. Since the grain size distribution is affected by hydrodynamical evolution of the ISM, we solve the evolution of grain size distribution based on hydrodynamical simulation results. We utilize the method developed by Hirashita & Aoyama (2019, hereafter HA19) for this purpose. We further include the formation of aromatic species as a result of photo-processing of (non-aromatic) HAC, rather than assuming small carbonaceous grains as PAHs.

This paper is organized as follows. In Section 2, we describe our PAH evolution model. In Section 3, we show the results and test them against observational data. In Section 4, we compare our new model with previous results (mainly S14), and describe future prospects. In Section 5, we give the conclusion of this paper.

2 MODEL

We use the evolution model of grain size distribution in HA19, which was developed based on Asano et al. (2013b). We post-process the hydrodynamical simulation of an isolated disc galaxy to derive the evolutionary paths of grain size distribution in various conditions of the ISM. In addition, we distinguish between aromatic and non-aromatic carbonaceous dust and consider the aromatization reaction from the second to the first species. For simplicity,

we only treat the evolution of carbonaceous dust (see Section 4 for further discussions on this point). In what follows, we explain our models.

2.1 Hydrodynamic simulation

We adopt the same hydrodynamic simulation as used in HA19. We only give a brief summary and refer the interested reader to HA19 for details. We use the modified version of GADGET3-OSAKA N -body/smoothed particle hydrodynamics (SPH) code (Aoyama et al. 2017; Shimizu et al. 2019; the original version of GADGET was introduced by Springel et al. 2005). We adopt the initial condition used in the low-resolution model of AGORA simulations (Kim et al. 2014, 2016). The following components are included in the initial condition: halo, stellar disc, gas disc, and bulge. The gas mass resolution is $8.6 \times 10^4 M_{\odot}$. The minimum gravitational softening length is 80 pc and the baryons are allowed to collapse to 10 per cent of this value. The star formation is assumed to occur in dense regions in a local free-fall time with an efficiency of 0.01. Stellar feedback and metal enrichment are calculated by CELib (Saitoh 2017), which includes both SNe and AGB stars.

The different evolution history of each SPH gas particle (hereafter, simply referred to as gas particle) could lead to different grain size distributions and PAH abundances. To concentrate on the typical galactic-disc region, we choose gas particles located at radii $0.1 < R < 4$ kpc and vertical height $-0.3 < z < 0.3$ kpc in the cylindrical coordinate (R, z) . Finally, we adopt 146 gas particles, which are sufficient to investigate the statistical properties.

2.2 Grain size distribution

We calculate the evolution of grain size distribution on each gas particle. We assume grains to be spherical and compact, so that $m = (4\pi/3)a^3s$, where m is the grain mass, a is the grain radius and s is the material density of dust. For simplicity, we assume that all the dust species are carbonaceous. We separate the carbonaceous species into aromatic and non-aromatic components, and concentrate only on these two carbonaceous species in this paper. We adopt the physical parameters (including the above grain density $s = 2.24 \text{ g cm}^{-3}$; see HA19 for the details in the material parameter dependence) appropriate for graphite for simplicity. Indeed, as we show later, quick aromatization would realize ordered structures rather than amorphous ones, which could justify the usage of graphite material properties. We neglect silicate to avoid complexity arising from inter-species interactions (e.g. collisions between silicate and carbonaceous grains). See Section 4.2 for more discussions on this assumption.

We define the grain size distribution at time t , $n_i(a, t)$, such that $n_i(a, t) da$ is the number density of grains with radius between a and $a + da$. The aromatic and non-aromatic species are specified by the index $i = \text{ar}$ and nonar , respectively. The total grain size distribution is indicated without an index as $n(a, t) \equiv n_{\text{ar}}(a, t) + n_{\text{nonar}}(a, t)$. The time evolution of the grain size distribution is driven by the following processes: dust condensation in stellar ejecta, dust destruction by SN shocks, grain disruption by shattering, dust growth by the accretion of gas-phase metals in the ISM, and grain growth by coagulation.

The stellar dust production is calculated based on the increase of the metallicity by assuming that a fraction $f_{\text{in}} = 0.1$ of newly injected metals from stars condense into dust. We assume that stars produce large ($a \sim 0.1 \mu\text{m}$) grains (more precisely, we assume a

lognormal grain size distribution centred at $a = 0.1 \mu\text{m}$ for dust grains produced by stars). All grains produced by stars are assumed to be non-aromatic (or we assume that the grains become aromatic only after being processed in the ISM).

Shattering and coagulation occur in the collisions between grains whose velocities are induced by interstellar turbulence (Yan et al. 2004). High and low turbulence velocities in the diffuse and dense ISM cause shattering and coagulation, respectively. Shattering and coagulation are treated based on the so-called Smoluchowski equation. We calculate shattering and coagulation separately for aromatic and non-aromatic species for simplicity (this simplification does not affect our results significantly). We assume that shattering only occurs in the diffuse phase with $n_{\text{H}} < 1 \text{ cm}^{-3}$ (n_{H} is the hydrogen number density) and that accretion and coagulation take place in the dense phase with $n_{\text{H}} > 10 \text{ cm}^{-3}$ and $T_{\text{gas}} < 1000 \text{ K}$ (T_{gas} is the gas temperature). Since the dense clouds where accretion and coagulation occur cannot be spatially resolved in our simulation, we assume that a mass fraction of $f_{\text{dense}} = 0.5$ in the dense phase is condensed into dense clouds with hydrogen number density 10^3 cm^{-3} and gas temperature 50 K on subgrid scales and that coagulation occurs only in those dense clouds.

The evolution of grain size distribution by accretion and SN destruction is governed by an advection equation in the a -space. We only treat accretion in the subgrid dense gas (i.e. coagulation and accretion take place in the same place). We apply the following procedure for accretion: we calculate the grain size distribution modified by accretion in the next time-step, $n(a, t + \Delta t)$. Since accreted material form non-aromatic structures (since we assume that aromatization occurs in the diffuse ISM; Section 2.3), we regard the increase of n at each a as the increase of n_{nonar} . Therefore, the non-aromatic grain size distribution is derived by $n_{\text{nonar}}(a, t + \Delta t) = n(a, t + \Delta t) - n_{\text{ar}}(a, t)$ if n_{nonar} is positive. In fact, it could become negative because accretion could decrease the dust abundance at the smallest a bins. In this case, we assume $n_{\text{nonar}} = n$ and $n_{\text{ar}} = 0$. For destruction, we count the SNe attacking the gas particle and assume that each SN destroys the dust contained in the swept medium with a grain-size-dependent efficiency given by HA19.

The total dust mass density $\rho_{\text{dust}}(t)$ is calculated by

$$\rho_{\text{dust}}(t) = \int_0^{\infty} \frac{4}{3} \pi a^3 s n(a, t) da. \quad (1)$$

The dust-to-gas ratio is estimated as $\rho_{\text{d,tot}}(t)/\rho_{\text{gas}}$, where $\rho_{\text{gas}} = \mu m_{\text{H}} n_{\text{H}}$ ($\mu = 1.4$ is the gas mass per hydrogen, and m_{H} is the mass of hydrogen atom).

In this paper, we neglect dust and PAH destructions by hard photons. It is likely that photo-destruction occurs only in regions near to the intense UV sources. Therefore, photo-destruction may not affect the dust properties in the entire galaxy compared with the dust processing mechanisms included above. Moreover, in the current simulation framework, a calculation of radiation field (or radiation transfer), which is generally computationally expensive, is not implemented. Photo-destruction also occurs selectively where the radiation field is hard; this means that we also need to trace the spatial/time variation of the hardness of stellar SED. Because of the local nature of photo-destruction and the technical difficulty, we focus on the interstellar processing mechanisms described above. Nevertheless, we include aromatization by the mean UV radiation field in the next subsection to justify that aromatic grains actually form on a short time-scale. Thus, we also address the photo-destruction by the mean UV field in Section 4.2.

2.3 Aromatization

Owing to photo-processing, grains lose mainly their hydrogen atoms. Herewith, the atomic structures change as mentioned above, and the material properties change correspondingly. In particular, the band gap energy, E_{g} , is related to the number fraction of hydrogen atoms (X_{H}) through $E_{\text{g}} = 4.3X_{\text{H}} \text{ eV}$ (Tamor & Wu 1990). When HAC grains are fully hydrogenated, E_{g} reaches the maximum value, 2.67 eV (Jones et al. 2013). In contrast, E_{g} has the minimum value when the grains are dehydrogenated. We assume that the minimum value of E_{g} is 0.1 eV . The maximum and the minimum values of E_{g} correspond to $X_{\text{H}} = 0.6$ and 0.02 , respectively. We define the aromatization time as the time necessary for dehydrogenation from the maximum value of X_{H} to the minimum one.

Based on Jones et al. (2014) and Murga et al. (2016a), we use the following expression for the time evolution of X_{H} for a grain:

$$\frac{dX_{\text{H}}}{dt} = Y_{\text{diss}}^{\text{CH}} \sigma_{\text{loss}}^{\text{CH}} \int_{10 \text{ eV}}^{13.6 \text{ eV}} Q_{\text{abs}}(a, E) F(E) dE, \quad (2)$$

where $Y_{\text{diss}}^{\text{CH}}$ is the dissociation probability for an incident photon on the grain, $\sigma_{\text{loss}}^{\text{CH}} (= 10^{-19} \text{ cm}^2)$ is the dissociation cross-section, $F(E)$ is the photon flux with energy E , and Q_{abs} is the absorption efficiency. We adopt $Y_{\text{diss}}^{\text{CH}} = 1$ for $a < 20 \text{ \AA}$ and $Y_{\text{diss}}^{\text{CH}} = 20 \text{ \AA}/a$ for $a \geq 20 \text{ \AA}$. We use the absorption cross-sections described originally by Jones (2012) and modified by Murga et al. (2019). The photon flux corresponds to the mean radiation field in the solar neighbourhood given by Mathis et al. (1983). This is valid for the purpose of examining the typical radiation field in Milky-Way-type galaxies. Also, our simulated galaxy has a constant star formation rate similar to the present Milky Way value ($\sim 1 M_{\odot} \text{ yr}^{-1}$). Finally, we obtain the following fitting formula for the aromatization time:

$$\frac{\tau_{\text{ar}}}{\text{yr}} = 3 \left(\frac{a}{\mu\text{m}} \right)^{-2} + 6.6 \times 10^7 \left(\frac{a}{\mu\text{m}} \right). \quad (3)$$

Since aromatization is associated with UV irradiation, we assume that it occurs in the diffuse ISM with $0.1 < n_{\text{H}} < 1 \text{ cm}^{-3}$, where UV radiation can penetrate easily. We define the aromatic fraction f_{ar} as

$$f_{\text{ar}}(a, t) \equiv n_{\text{ar}}(a, t)/n(a, t), \quad (4)$$

and calculate its time evolution as

$$\frac{\partial f_{\text{ar}}}{\partial t} = (1 - f_{\text{ar}})/\tau_{\text{ar}}. \quad (5)$$

Following S14, we assume the grain radii of PAHs to be between $a_{\text{PAH,min}} = 3 \times 10^{-4}$ and $a_{\text{PAH,max}} = 2 \times 10^{-3} \mu\text{m}$, corresponding to ~ 20 – 3000 carbon atoms. We calculate the mass density of PAHs, ρ_{PAH} , as

$$\rho_{\text{PAH}}(t) = \int_{a_{\text{PAH,min}}}^{a_{\text{PAH,max}}} f_{\text{ar}}(a, t) \rho_{\text{dust}}(a, t) da. \quad (6)$$

As clarified in the Introduction, we assume that small aromatized grains are the carriers of the MIR features. It is not necessary, however, to specify the optical properties of large aromatized grains in this paper. We expect that large aromatized grains do not show prominent mid-infrared features. As shown by Murga et al. (2016b), aromatic grains do not show MIR features if grain radii are larger than $\sim 100 \text{ \AA}$. Since we categorize carbonaceous grains with regular ring-like structures as aromatized grains, graphite could also be regarded as ‘aromatized’ grains in our model. Detailed specification of the material properties for large aromatized grains is left for future work.

3 RESULTS

3.1 Grain size distribution and aromatic fraction

Since we already discussed the evolution of grain size distribution in HA19, we only give a brief summary of it. The evolutionary trend of grain size distribution is similar among the gas particles; thus, we show only two chosen cases (Fig. 1). To show the effect of dust growth by accretion, we chose a case where the bump created by accretion is clearly seen (upper panel of Fig. 1). At the earliest stage ($t \lesssim 0.3$ Gyr), stellar dust production dominates the dust abundance; thus, the grain size distribution follows the lognormal distribution of dust grains produced by stars. At $t \gtrsim 0.3$ Gyr, shattering produces a tail towards small grain radii. At $t \gtrsim 1$ Gyr, dust growth by accretion drastically increases the small grain abundance because accretion is more efficient for smaller grains, which have larger surface-to-volume ratios. Accretion often creates a prominent bump around $a \sim 0.01 \mu\text{m}$ as observed in the upper panel of Fig. 1. At $t \gtrsim 3$ Gyr, coagulation converts small grains to large ones, contributing to the increase of the large-grain abundance.

We also show the aromatic fraction (f_{ar}) in the lower window of each panel. We observe that f_{ar} is almost 1 for $a \lesssim 0.1 \mu\text{m}$ at all ages. This is due to the short aromatization time-scale. However, for the case shown in the upper panel in Fig. 1, the aromatic fractions at $t = 0.3$ and 3 Gyr have the minimum value at $a \sim 10^{-3} \mu\text{m}$ and at $a \sim 10^{-2} \mu\text{m}$, respectively, where the grain size distribution also has a peak. This peak is caused by accretion as mentioned above. Recall that accretion is assumed to contribute to the increase of non-aromatic grains (Section 2.2). As shown in equation (3), the aromatization time-scale in the radius regime of PAHs is $\sim 10^6$ – 10^7 yr. The accretion time-scale can be as short as 10^6 yr at $a \sim 10^{-3} \mu\text{m}$ at solar metallicity (HA19). This explains the temporary drop of aromatic fraction in the phase of efficient accretion. Since accretion occurs on a short time-scale, the aromatic fraction temporarily drops. However, aromatization quickly occurs subsequently, and the aromatization time-scale is still much shorter than the overall dust enrichment time-scale (\sim chemical enrichment time-scale). Thus, we do not observe low aromatic fractions in most of the cases. Except for the phase of rapid accretion in the dense ISM, we can practically regard the production of small carbonaceous grains as the PAH formation.

3.2 PAH abundance and metallicity

Now we investigate the evolution of PAH abundance. First, we examine the dust-to-gas ratio $\rho_{\text{dust}}/\rho_{\text{gas}}$ in Fig. 2 since the total abundance of dust, from which PAHs form in our model, is a basic quantity for the interpretation of the PAH abundance. For the indicators of PAH abundance, we examine the PAH-to-gas ratio ($\rho_{\text{PAH}}/\rho_{\text{gas}}$) in Fig. 3 and the PAH-to-dust ratio ($\rho_{\text{PAH}}/\rho_{\text{dust}}$) in Fig. 4. Metallicity is used as an indicator of evolutionary stage. Indeed, the relation between dust-to-gas ratio and metallicity has been used to investigate the dust enrichment processes (Issa et al. 1990; Schmidt & Boller 1993; Lisenfeld & Ferrara 1998; Dwek 1998; Rémy-Ruyer et al. 2014). We used all the snapshots (output every 10^7 yr) for the sampled gas particles to derive the following statistical properties. We divided metallicity into 40 linear bins, and show the medians in these bins in the figures. The number of data points in each bin is around 10^3 . The shaded regions represent the area between the first and third quartiles. We also compare the results with the data of nearby galaxies compiled by S14 (originally taken from Galliano et al. 2008 and Draine et al. 2007). The observational metallicity data are based on the oxygen abundance. Thus,

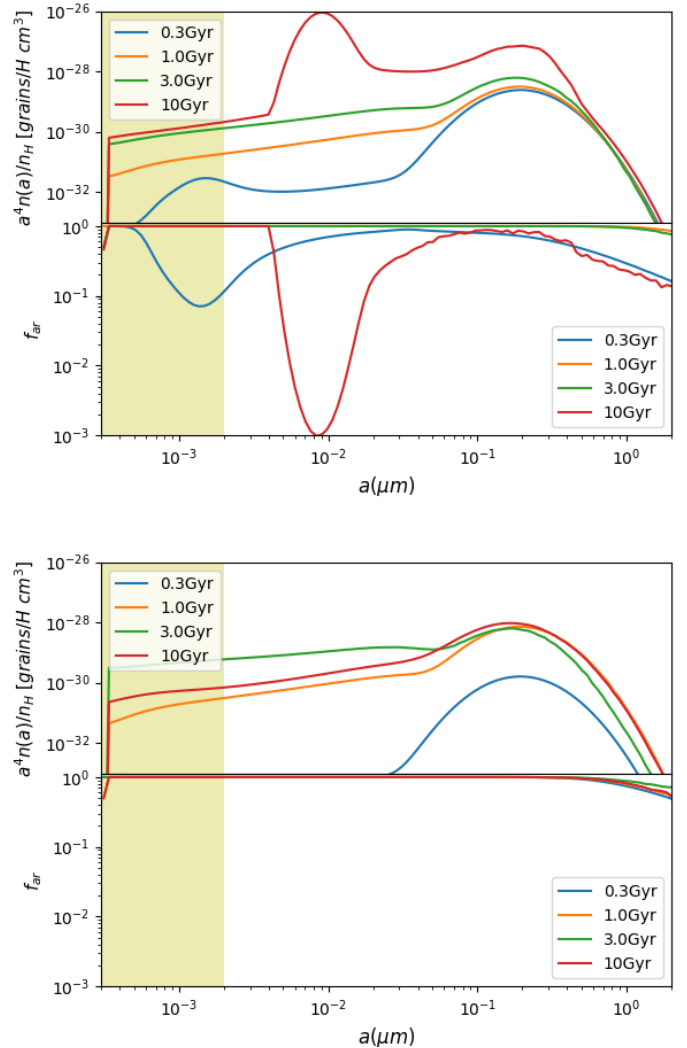


Figure 1. Evolution of grain size distribution and aromatic fraction (f_{ar}) for two of the gas particles. The upper and lower parts in each panel are the grain size distribution per hydrogen multiplied by a^4 (this quantity is proportional to the grain mass distribution per $\log a$), and the aromatic fraction (f_{ar}), respectively. The different lines represent the different ages as shown in the legend. The shaded region shows the radius range of PAHs.

we assume that the oxygen abundance fairly traces the total metallicity. The solar oxygen abundance is uncertain, and we simply followed the solar abundance values adopted in those original papers ($12 + \log(\text{O}/\text{H})_{\odot} = 8.83$ and $12 + \log(\text{O}/\text{H})_{\odot} = 8.69$ for Galliano et al. 2008 and Draine et al. 2007, respectively), keeping in mind that there is a factor 2 uncertainty in the solar metallicity. The typical error of the PAH abundance is a factor of ~ 2 . Note that each of their data points represents an individual galaxy. Here we regard our results on the gas particles as representing the evolution of PAH abundance in galaxies with a variety of physical conditions. In our post-processing procedure, it is not possible to derive the global quantities. We expect that the global dust and PAH abundances lie near the medians or at least within the shaded regions in the diagrams.

We observe in Fig. 2 that the dust-to-gas ratio increases with

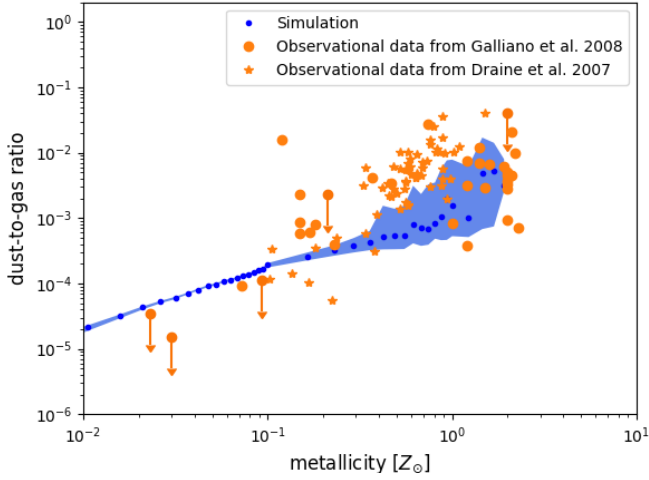


Figure 2. Relation between dust-to-gas ratio and metallicity. The blue points are the median of our simulations in the metallicity bins with blue regions showing the area between the first and third quartiles. The orange points show the observational data for nearby galaxy samples taken from Galliano et al. (2008) and Draine et al. (2007). The typical error of dust abundance is smaller than a factor of 2. Note that there is also a factor 2 systematic uncertainty in solar metallicity, which causes a shift of the observational data in the horizontal direction.

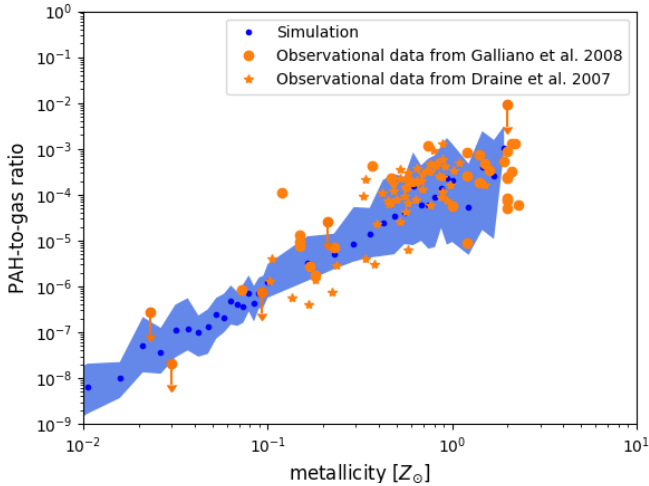


Figure 3. PAH-to-gas mass ratio as the function of metallicity. The blue points are the median of our simulations in the metallicity bins with blue regions showing the area between the first and third quartiles. The orange points show the data for the same observational samples as adopted in Fig. 2. The typical error of the PAH abundance is a factor of 2.

metallicity. This is a natural consequence of chemical enrichment and metal accretion on dust. Most of the observational data points are consistent with the simulation result. The dust-to-gas ratio has very small dispersion at low metallicity ($Z \lesssim 0.1 Z_{\odot}$) because the dust-to-metal ratio is always $\sim f_{\text{in}}$ determined by the condensation efficiency in stellar ejecta in our model. A nonlinear increase and an expansion of dispersion are apparent at high metallicity. This

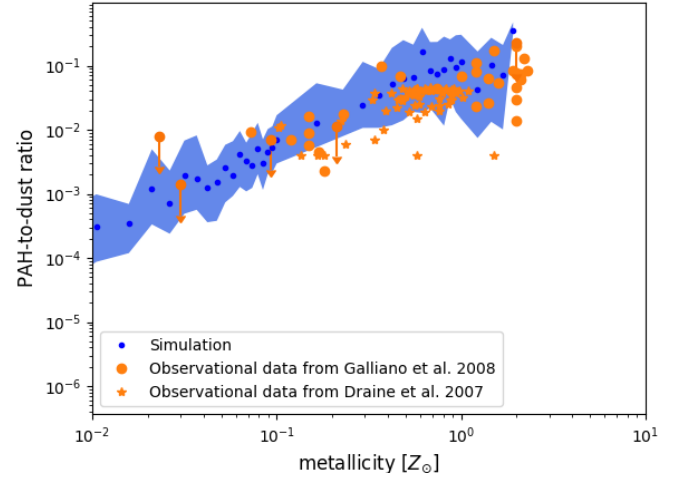


Figure 4. PAH-to-dust mass ratio as function of metallicity. The blue points are the medians in the metallicity bins with blue regions showing the area between the first and third quartiles for our simulation results. The orange points present the data for the same observational samples as adopted in Fig. 2. The typical error of the PAH abundance is a factor of 2.

behaviour at high metallicity is caused by accretion (dust growth) (Dwek 1998; Hirashita 1999; Zhukovska et al. 2008). We tend to underestimate the dust-to-gas ratio at subsolar metallicity (~ 0.2 – $0.5 Z_{\odot}$), but this may be due to the effect of averaging. Observational dust abundance is derived in a luminosity-weighted way, which could be more biased to dust-rich regions associated with star-forming regions, while we treat all the sampled gas particles equally. However, we should emphasize that our model successfully covers a large part of the observed dust-to-gas ratios at high metallicity.

Next, we examine the relation between PAH-to-gas ratio ($\rho_{\text{PAH}}/\rho_{\text{gas}}$) and metallicity in Fig. 3. Our model reproduces the observed relation. The increase of PAH abundance coincides with that of dust-to-gas ratio as expected, but the increase of PAH abundance along the metallicity is steeper than that of dust-to-gas ratio. For the purpose of showing this steep increase of PAH abundance, we show the evolution of PAH-to-dust ratio ($\rho_{\text{PAH}}/\rho_{\text{d,tot}}$) in Fig. 4. Our calculation shows the increase of PAH-to-dust ratio with metallicity. The increase is quantitatively consistent with the observational data. The increase of PAH-to-dust ratio indicates that the PAH abundance is more sensitive to the metallicity than the total dust abundance is. Since PAHs originate from small grains in our model, shattering and accretion are important for PAH formation. Accretion does not form PAHs directly, but it enhances the abundance of small non-aromatic grains, which are subsequently converted to aromatic species. Since the efficiencies of both accretion and shattering depend on the dust abundance (and metallicity for accretion), the increase of small grains has a nonlinear dependence on the metallicity (Hirashita 2015); in other words, the increase of small grains is more sensitive to the metallicity than that of the total dust abundance. This is why the PAH-to-dust ratio increases with the metallicity.

4 DISCUSSION

4.1 Comparison with the previous model

S14 modelled the evolution of PAH abundance by post-processing the dust-to-gas ratio calculated separately. They assumed shattering to be the source of PAHs. We focus on their model with the nearest star formation time-scale, $\tau_{\text{SF}} = 5$ Gyr, to our simulated galaxy. The evolution of PAH abundance in S14 shows a steep increase at $Z \sim 0.2 Z_{\odot}$. This is a natural consequence of accretion, which drastically raise the dust abundance at sub-solar metallicity. S14 has a steeper increase of PAH abundance at $Z < 0.2 Z_{\odot}$ than our results, which is also due to their steeper increase of dust-to-gas ratio. In a one-zone model like S14, the rapid increase of dust and PAH abundances by accretion occurs at a certain metallicity, while in our spatially resolved modelling, the rapid increase does not occur coherently. As a consequence, the increase of PAH abundance becomes milder in our model than in S14.

We calculated the grain size distribution, while S14 did not. Accretion as well as shattering directly increases the small-grain abundance. The rate of small-grain formation is treated in a consistent manner with the evolution of grain size distribution in our model. Although our results are qualitatively similar to S14's, the treatment of grain size distribution is still essential since the rates of shattering and accretion strongly depends on the grain size distribution.

Previous studies suggest other evolutionary pictures for PAH abundance. Broadly, there are two major possibilities: destruction by SNe and PAH supply by AGB stars. O'Halloran et al. (2006) showed a prominent anticorrelation between the $7.7 \mu\text{m}$ feature strength, which is an indicator of the PAH abundance, and the $[\text{Fe II}]/[\text{Ne II}]$ line ratio, which is a tracer of SN shocks. They also found an anticorrelation between the $[\text{Fe II}]/[\text{Ne II}]$ ratio and metallicity, arguing that the strong destruction of PAHs by SN shocks could be the cause of the deficiency of PAHs in low-metallicity galaxies. We included shock destruction in our calculations, but found that shattering still continuously supply small grains, which are quickly aromatized. In our model, shattering occurs everywhere in the diffuse ISM because of the turbulent motion (see also Yan et al. 2004; Hirashita & Yan 2009). Jones et al. (1996) showed that grains are not only sputtered but also shattered in SN shocks. Shattering in SN shocks could be as efficient as shattering in interstellar turbulence (Hirashita et al. 2010). Therefore, it cannot be simply concluded that the enhanced SN rate leads to a depletion of PAHs. For the other possibility (PAH supply by AGB stars), Galliano et al. (2008) and Bekki (2013) assumed that the PAH abundance is governed by the ejection of carbonaceous dust from AGB stars. In their models, the paucity of PAHs in low-metallicity galaxies is explained by young ages (i.e. lack of AGB stars). Although our results do not exclude these possible explanation for the PAH–metallicity correlation, we emphasize that our model naturally predicts it since the small-grain production is sensitive to the metallicity.

4.2 Caveats and future prospects

In our model, we only treated the carbonaceous species for simplicity. In the Galactic environment, it is known that the interstellar dust contains as much silicate as carbonaceous dust (e.g. Weingartner & Draine 2001). However, how these two species interact is not certain. They may evolve separately or make compound species. Experimental studies of dust growth could help to resolve this issue (Rouillé et al. 2015). It is also suggested that carbonaceous materials could coat silicate grains (Jones et al. 2017). In this case,

silicate grains act as a ‘host’ of the growth of carbonaceous grains in the sense that silicate grains accrete carbonaceous materials to form grains whose optical properties eventually resemble pure carbonaceous grains. If these coated grains are shattered (note also that there could be other mechanisms of grain disruption; Hoang 2019), we expect that small carbonaceous dust is injected into the ISM. Therefore, we expect that our simplified treatment in this paper is still meaningful in the presence of silicate.

The inverse reaction of aromatization, ‘aliphaticization’, could also happen. This inverse process is also possible when the rate of dehydrogenation is lower than that of hydrogen accretion on the grain surface. As the C–C bonds become aliphatic after attachment of new atoms, the material structures are transformed from ordered to disordered ones. Aliphaticization is expected to occur in weak UV radiation field and high hydrogen density. Jones et al. (2014) found that this process is efficient where the visual extinction is in the range of $0.01-0.7 \leq A_V \leq 1.5$ (the lower limit depends on the incident radiation field intensity). On the other hand, we already included the formation of amorphous grains through metal accretion in the dense ISM. Aliphaticization is also taken as an accretion process of hydrogen, so that we can effectively include aliphaticization into accretion in our framework. We have shown that formed non-aromatic grains are aromatized quickly. Thus, we expect that, even if we include the inverse reaction, our results are not altered significantly because of the quick aromatization. Moreover, since our results without aliphaticization is consistent with the observed PAH abundances, we could argue that aliphaticization is not likely to play a dominant role in determining the PAH abundance in nearby galaxies.

In this paper, we neglected photo-destruction, which is likely to be effective only locally (Section 2.2). Nevertheless, even the mean radiation field could destroy the smallest PAHs. This destruction may systematically decrease the abundance of PAHs at all metallicities compared with our calculation results. According to Murga et al. (2016a), for the radiation field given by Mathis et al. (1983), the destruction time-scale for PAHs smaller than $a \sim 5 \text{ \AA}$ is shorter than $\sim 10^9$ yr (dust enrichment time-scale). However, even if all the PAHs with $a \leq 5 \text{ \AA}$ are eliminated in our calculations, it decreases the PAH abundance by at most 20 per cent. Therefore, the photo-destruction by the mean radiation field does not affect our results significantly.

As a natural extension of our modelling, we could calculate the evolution of PAH abundance and the hydrodynamical development of the ISM simultaneously. This step serves to clarify the distribution of PAHs within a galaxy. Indeed, there have already been some hydrodynamical simulations that include the evolution of grain size distribution (McKinnon et al. 2018; Aoyama et al. 2019). In addition, incorporating aromatization in the simulation framework is necessary to complete this extension.

5 CONCLUSION

We post-process a previous hydrodynamical simulation of an isolated galaxy with our evolution model of PAHs. We calculate the evolution of PAH abundance in a consistent manner with the evolution of grain size distribution. We also explicitly include aromatization. In this model, the main PAH formation path is the interplay between shattering and accretion and the subsequent aromatization. We find that aromatization occurs quickly so that the formation of small carbonaceous grains could be regarded as the production of PAHs. Carbonaceous grains could be non-aromatic only in the

phase of rapid dust growth by metal accretion in the dense ISM, while they are aromatic in most of the galaxy evolution stages.

We find that the calculated relations between PAH abundance (PAH-to-gas ratio and PAH-to-dust ratio) and metallicity are consistent with the observation data of nearby galaxies. In particular, the nonlinearity of shattering and accretion in terms of the metallicity naturally explains the nonlinear increase of the PAH abundance as a function of metallicity. The dispersion of PAH abundances is interpreted as caused by a variety in the physical conditions (gas density, temperature, etc.) of the ISM. We conclude that the scenario that PAHs form as a result of small-grain production by shattering and accretion with subsequent aromatization explains the observed strong metallicity dependence of PAH abundance.

ACKNOWLEDGEMENTS

We are grateful to the anonymous referee for useful comments. We thank S. Aoyama for providing us with the hydrodynamic simulation data, and J. Y. Seok for sending us the compiled data of nearby galaxies. HH thanks the Ministry of Science and Technology for support through grant MOST 105-2112-M-001-027-MY3 and MOST 107-2923-M-001-003-MY3. MM acknowledges the support from the RFBR grant 18-52-52-006.

REFERENCES

- Allamandola L. J., Tielens A. G. G. M., Barker J. R., 1985, *ApJ*, 290, L25
Aoyama S., Hirashita H., Nagamine K., 2019, *MNRAS*, submitted (arXiv:1906.01917)
Aoyama S., Hou K.-C., Shimizu I., Hirashita H., Todoroki K., Choi J.-H., Nagamine K., 2017, *MNRAS*, 466, 105
Asano R.S., Takeuchi T.T., Hirashita H., Inoue A.K., 2013a, *Earth Planets Space*, 65, 213
Asano R.S., Takeuchi T.T., Hirashita H., Nozawa T., 2013b, *MNRAS*, 432, 637
Bekki K., 2013, *MNRAS*, 432, 2298
Cherchneff I., Barker J. R., Tielens A. G. G. M., 1992, *ApJ*, 401, 269
Ciesla, L., et al., 2014, *A&A*, 565, A128
Draine B. T. et al., 2007, *ApJ*, 663, 866
Duley W. W., 1993, in S. Kwok, ed, *ASP Conf. Ser. Vol. 41, Astronomical Infrared Spectroscopy: Future Observational Directions*, ASP, San Francisco, p. 241
Duley W. W., Zaidi A., Wesolowski M. J., Kuzmin, S., 2015, *MNRAS*, 447, 1242
Dwek E., 1998, *ApJ*, 501, 643
Engelbracht C. W., Gordon K. D., Rieke G. H., Werner M. W., Dale D. A., Latter W. B., 2005, *ApJ*, 628, L29
Förster Schreiber N. M., Roussel H., Sauvage M., Charmandaris V., 2004, *A&A*, 419, 501
Galliano F., Dwek E., Chantal P., 2008, *ApJ*, 672, 214
Hirashita H., 1999, *ApJ*, 510, L99
Hirashita H., 2015, *MNRAS*, 447, 2937
Hirashita H., 2012, *MNRAS*, 422, 1263
Hirashita H., Aoyama S., 2019, *MNRAS*, 482, 2555 (HA19)
Hirashita H., Nozawa T., Yan H., Kozasa T., 2010, *MNRAS*, 404, 1437
Hirashita H., Yan H., 2009, *MNRAS*, 394, 1061
Hoang T., 2019, *ApJ*, 876, 13
Hou K.-C., Hirashita H., Nagamine K., Aoyama S., Shimizu I., 2017, *MNRAS*, 469, 870
Hunt L. K., Thuan T. X., Izotov Y. I., Sauvage M., 2010, *ApJ*, 712, 164
Issa M. R., MacLaren I., Wolfendale A. W., 1990, *A&A*, 236, 237
Jones A.-P., 2012, *A&A*, 542, A98
Jones A.-P., Köhler M., Ysard N., Bocchio M., Verstraete L., 2017, *A&A*, 602, A46
Jones A. P., Fanciullo L., Köhler M., Verstraete L., Guillet V., Bocchio M., Ysard N., 2013, *A&A*, 558, A62
Jones A. P., Tielens A. G. G. M., Hollenbach D. J., 1996, *ApJ*, 469, 740
Jones, A. P., Ysard N., Köhler M., Fanciullo L., Bocchio M., Micelotta E., Verstraete L., Guillet V., 2014, *Faraday Discussions*, 168, 313
Kim J.-h. et al., 2014, *ApJS*, 210, 14
Kim J.-h. et al., 2016, *ApJ*, 833, 202
Kunth D., Östlin G., 2000, *A&ARv*, 10, 1
Kwok S., Zhang Y., 2011, *Nature*, 7371, 80
Leger A., Puget J. L. *A&A* 137, L5-L8
Li A., Draine B. T., 2012, *ApJ*, 760, L35
Lisenfeld U., Ferrara A., 1998, *ApJ*, 496, 145
Madden S. C., 2000, *New Astronomy Reviews*, 44, 249
Madden S. C., et al. 2006, *A&A*, 446, 877
Mathis J. S., Mezger P. G., Panagia N., 1983, *A&A*, 128, 212
Mathis J.S., Rumpl W., Nordsieck K.H., 1977, *ApJ*, 217, 425
McKinnon R., Vogelsberger M., Torrey P., Marinacci F., Kannan R., 2018, *MNRAS*, 478, 2851
Murga M. S., Khoperskov S. A., Wiebe D. S., 2016a, *Astronomy Reports*, 60, 233
Murga M. S., Khoperskov S. A., Wiebe D. S., 2016b, *Astronomy Reports*, 60, 669
Murga, M. S., Wiebe, D. S., Sivkova, E. E., et al. 2019, *MNRAS*, 488, 965
O’Halloran B., Satyapal S., Dudik R. P., 2006, *ApJ*, 641, 795
Rouillé G., Jäger C., Krasnokutski S. A., 2015, *Faraday Discussions*, 168, 449
Sandstrom, K. M., et al., 2012, *ApJ*, 744, 20
Saitoh T. R., 2017, *AJ*, 153, 85
Sakata A., Wada S., Tanabe T., Onaka T., 1983, *ApJ*, 287, L51
Schmidt K.-H., Boller T., 1993, *Astronomische Nachrichten*, 314, 361
Seok J. Y., Hirashita H., Asano R. S., 2014, *MNRAS*, 439, 2186 (S14)
Shimizu I., Todoroki K., Yajima H., Nagamine K., 2019, *MNRAS*, 484, 2632
Shivaei I., et al., 2017, *ApJ*, 837, 157
Springel V., 2005, *MNRAS*, 364, 1105
Plante S., Sauvage M., 2002, *AJ*, 124, 1995
Rémy-Ruyer A., et al., 2014, *A&A*, 563, A31
Tamor M. A., Wu C. H., 1990, *Journal of Applied Physics*, 67, 1007
Tielens A. G. G. M., 2008, *ARA & A*, 46, 289
Weingartner J. C., Draine B.T., 2001, *ApJ*, 548, 296
Wu Y., Charmandaris V., Hao L., Brandl B. R., Bernard-Salas J., Spoon H. W. W., Houck J. R. 2006, *ApJ*, 639, 157
Yan H., Lazarian A., Draine B. T., 2004, *ApJ*, 616, 895
Zhukovska S., Gail H.-P., Trieloff M., 2008, *A&A*, 2008, 479, 453

This paper has been typeset from a $\text{\TeX}/\text{\LaTeX}$ file prepared by the author.